Energy Tracing of Photovoltaic Cells

Yidan An, Tianshu Ma, and Xiaofeng Li*

Where did the solar energy go in photovoltaic cells in addition to the electricity? Herein, a detailed analytical derivation and numerical investigation on tracing the energy in solar cells (SCs) driven by various mechanisms are presented. Particularly, the critical factors constraining the SC performance are addressed, i.e., the energy and voltage losses. Six categories of intrinsic losses and three categories of potential losses in SCs are identified, in which the sum of Joule and Peltier losses show a constant under a specific bias and can be regarded as a self-heating effect within SC; moreover, it is strongly dependent with the key material/device parameters, which can be effectively decreased for a realistic (with carrier recombination) SC system so that approaches the limiting efficiency. To bridge the energy loss and the temperature characteristics, an opto–electro–thermal model is developed to accurately mimic the multiphysics responses of SCs. For Si/perovskite and perovskite/perovskite double-junction SCs, the energy-tracing study explains the various energy factors limiting the highest efficiency and predicts an efficiency up to 37.5% by an optimal Si/perovskite double-junction design. The energy-based study promotes the understanding of the fundamental photovoltaic physics for the possibilities of new photoconversion strategies with higher performances.

1. Introduction

During the past decades, extensive efforts in developing high-efficiency solar cells (SCs) witnessed a continuous record breaking in the achievable highest efficiency.[1–6] So far, the laboratory efficiencies of 26.3% and 29.1% have been achieved for single-junction Si and double-junction Si/perovskite SCs, respectively.[1,5] However, a thermodynamic estimation reveals that the theoretical efficiencies of single- and double-junction SCs can be up to 33% and 45%, respectively.[7,8] The noticeable gap arises from the huge carrier thermodynamic losses in SCs, which are converted directly or indirectly into heats. A deep understanding on the fundamental carrier thermodynamic behaviors in various SCs, e.g., in single- or double-junction systems, is of high significance.

For years, accurately predicting the limiting performance of SCs with uncovering the details of the various energy losses has attracted considerable attention. For example, Shockley and Queisser predicted the limiting efficiency of a single-junction SC (SQ limit) with the highest efficiency of 30% using the photovoltaic material with the bandgap of 1.1 eV.[7] Based on the generalized Planck equation, the intrinsic losses of transmission, thermalization, emission, Carnot, and Boltzmann losses were demonstrated to be the key factors constraining the efficiency of SC.[9] There were many studies focusing on the loss origins of efficiency and open-circuit voltage (V_{oc}) by quantifying the carrier loss processes within SCs. It was discovered that the carrier recombination critically limits the V_{oc}, so that the performances of the practical SCs are far from the theoretical expectation.[10–14] By constructing the advanced heterojunction interface (e.g., interface passivation and energy-band alignment), the interface recombination can be effectively diminished to obtain a favorable carrier transportation.[15,16] We also developed an optoelectronic model to quantitatively analyze the carrier loss channels,[17–20] and further identified the typical carrier thermodynamic losses by constructing an opto–electro–thermal (OET) model for better understanding the SCs.[21,22]

All these efforts were closely related to an open question: "where did the solar energy go besides generating the electricity?" Only with obtaining the thermodynamic details in SCs, it is then possible to figure out the effective strategies to maximize the electrical output. To fully exploit the thermodynamic fundamentals and guide the design of high-performance SCs, a thorough study on the physical origins of intrinsic losses during the energy-conversion processes is highly required.[23–25] This motivates us to "trace" the various energies (electricity and heat losses) in photovoltaic cells. We believe that such a study should be grounded on the analytical derivation, which sorts out the intrinsic physical relationships of the critical energy components.[25] Then, before the experiment, it is necessary to conduct a complete multiphysics study to numerically address the optical, electrical, and thermodynamic responses as well as provide the detailed map of the various energy components in SCs.

Y. An, T. Ma, Prof. X. Li
School of Optoelectronic Science and Engineering & Collaborative Innovation Center of Suzhou Nano Science and Technology
Soochow University
Suzhou 215006, China
E-mail: xfli@suda.edu.cn

Y. An, T. Ma, Prof. X. Li
Key Lab of Advanced Optical Manufacturing Technologies of Jiangsu Province & Key Lab of Modern Optical Technologies of Education Ministry of China
Soochow University
Suzhou 215006, China

In this article, we study the intrinsic energy-conversion mechanisms with especially addressing the origins of energy and voltage losses in single- and double-junction SCs. The carrier thermodynamic processes are analytically derived and numerically studied to trace the channels of energy losses and voltage drops in SCs. We comparably studied the effect of key material/device parameters (e.g., recombination, doping concentration, and energy band offset) on the energy components and open-circuit voltage for the limiting and realistic performances of SCs. We then develop a coupled OET model to estimate the working temperature and temperature-dependent limiting efficiency of single-junction SCs. Applying the OET analysis, we further investigate the energy-conversion issues of double-junction SCs, so that the best bandgap-matched double-junction SCs can be obtained. Such a thermodynamic study is beneficial for understanding the photovoltaic fundamentals as well as guiding the design of high-performance SCs.

2. The Modeling Methods

2.1. Analytically Tracing the Energies in Single-Junction SCs

2.1.1. Energy Losses

Based on the detailed balance theory, the limiting efficiency of a SC can be achieved based on the following fundamental hypotheses: 1) optically, the incident photons with energy above the material bandgap ($h\nu > E_g$) are perfectly absorbed, and those below the bandgap ($h\nu < E_g$) are lost by transmission; 2) electrically, one absorbed photon precisely generates one electron–hole pair and only the radiative recombination results in the annihilation of photogenerated carriers; 3) thermally, the excessive photon energy does not heat the SC, which therefore has a temperature identical to the ambient (e.g., 300 K).[7,26] Based on these hypotheses, we investigate the carrier transportation and thermodynamic conversion processes of SCs under three junction configurations

(i.e., pn homojunction, pn heterojunction, and pin heterojunction), as shown in **Figure 1**. More generally, six categories of energy relaxations are addressed in heterojunction SCs as follows[21,22]: 1) thermalization (H_{therma}) arising from the excess kinetic energy loss of generated hot-carrier on subpicosecond timescales; 2) Joule heat (H_{Joule}) caused by the carrier potential drop due to the energy band shift; 3) Peltier heat at semiconductor–semiconductor (heterojunction) interface ($H_{Peltier}^{SS}$) due to the energy band offset; 4) Peltier heat at the metal–semiconductor interface ($H_{Peltier}^{SM}$) arising from the electron (hole) energy relaxation from the conduction (valence) band to the corresponding quasi-Fermi level; 5) bulk recombination (H_{Rec}^{Bulk}) caused by the typical bulk recombination losses (e.g., Shockley–Read–Hall, Auger, and radiation recombinations); and 6) surface recombination (H_{Rec}^{surf}) caused by the minority carrier losses at the surface of SC due to the surface trap or defect. It should be noted that there was no Peltier heat at the semiconductor–semiconductor interface in the homojunction SC (see S1, Supporting Information).

Under the illumination, the photogenerated carriers with energy of $h\nu$ released the excess energy into the material lattice and relax to the vicinity of 1) the bottom of the conduction band (i.e., $1.5k_BT + E_c$) or 2) the top of the valence band (i.e., $E_v - 1.5k_BT$), i.e., the thermalization process. These photogenerated carriers were then transported to the corresponding electrodes under the driving force of built-in electric field. If there were no carrier recombinations, the photogenerated carriers would be perfectly converted into the collected electrons, generating photocurrent J_{ph}; however, with carrier recombination losses, the actual photocurrent would be degraded into J ($<J_{ph}$), i.e., the overall carrier recombination process. Then the rest carrier potential energy would go to the Joule and Peltier heats, i.e., with combing the Equation (S2) and (S4)–(S7), Supporting Information, for the unbiased pn homojunction or pin heterojunction system, the sum of Joule and Peltier losses can be written as

$$H_{Joule} + H_{Peltier}^{SM} + H_{Peltier}^{SS} = (E_g + 3k_BT) \cdot J/q \qquad (1)$$
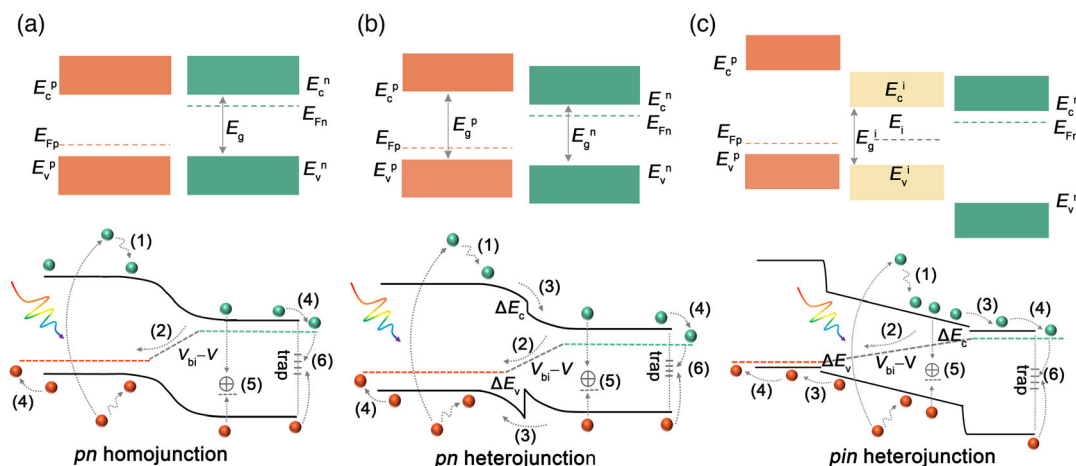

Figure 1. The schematic diagrams of the thermodynamic conversion processes of photogenerated carriers in a) pn homojunction, b) pn heterojunction, and c) pin heterojunction system, where the heat processes are: 1) thermalization, 2) Joule heat, 3) Peltier heat at heterojunction interface, 4) Peltier heat at the metal–semiconductor interface, 5) bulk recombination, and 6) surface recombination.

where $3k_BT$ is the thermal average kinetic energy of the carriers and q the charge constant.[27] It should be noted that the energy losses due to carrier recombinations have been automatically included in Equation (1) due to the use of J instead of J_{ph}.

Similarly, for the unbiased pn heterojunction, we have

$$H_{Joule} + H_{Peltier}^{SM} + H_{Peltier}^{SS} = [\max(E_g^n, E_g^p)/q + 3k_BT] \cdot J/q \quad (2)$$

where the E_g^n (E_g^p) is the bandgap of n(p)-type material. It is very interesting that the sum of the Joule and Peltier losses is determined only by the bandgap of photovoltaic layer and the current within the junction.

If applying a forward electrical bias of V, the Joule heat was reduced to $(V_{bi} - V) \cdot J$, where V_{bi} is the initial built-in potential difference $\left[V_{bi} = \frac{k_BT}{q}\ln\left(\frac{N_aN_d}{n_i^2}\right)\right]$.[28] Thus, with combing the Equation (S3)–(S7), Supporting Information, the sum of Joule and Peltier energies can be redefined as

$$H_{Joule} + H_{Peltier}^{SM} + H_{Peltier}^{SS} = (E_g + 3k_BT - qV) \cdot J/q \quad (3)$$

In this case, the sum of the Joule and Peltier losses was now determined by the forward bias, current and material bandgap, and the potential energy loss was $E_g + 3k_BT - qV$ before successfully collecting the carrier under a forward bias V. That is to say, to effectively drive the carrier transportation/separation/collection under the pn junction, the inevitable energy losses were obtained within the SC (named intrinsic self-heating effect), which was independent with the junction type (e.g., pn homojunction and pn/pin heterojunction).

2.1.2. Voltage Losses

From the carrier potential viewpoint, we can have

$$V_{Joule} + V_{Peltier}^{SM} + V_{Peltier}^{SS} = (E_g + 3k_BT)/q - V \quad (4)$$

where V_{Joule}, $V_{Peltier}^{SM}$ and $V_{Peltier}^{SS}$ are the potential drops caused by the Joule heat, Peltier heat at metal–semiconductor interface, and Peltier heat at heterojunction interface, respectively. It showed that the Joule and Peltier processes reduce the carrier potential from E_g/q to V. With using the Equation (4), the open-circuit voltage can be derived

$$V_{oc} = E_g/q + 3k_BT - V_{Joule} - (\Delta\varphi_n + \Delta\varphi_p)/q \\ - (\Delta E_c + \Delta E_v)/q \quad (5)$$

where $V_{Joule} = V_{bi} - V$ is the energy band shift in the depletion region, $\Delta\varphi_n = E_c - E_{Fn}$ ($\Delta\varphi_p = E_{Fp} - E_v$) the lost potential energy of the electron (hole) at the metal–semiconductor interface, $\Delta E_c = E_c^i - E_c^n$ ($\Delta E_v = E_v^p - E_v^i$) the lost potential energy of the electron (hole) at the heterojunction interface (see Figure 1c).

Here, we can have a more detailed discussion on the terms limiting the value of V_{oc}. i) Under the open-circuit situation, the generation (G) will balance with the recombination ($\gamma np = G$, where γ is the recombination rate, n the electron concentration, and p the hole concentration)[12,13] and the forward bias is equivalent to the splitting of Fermi level $\left[\text{e.g., } V = \frac{E_{Fn} - E_{Fp}}{q} = \frac{k_BT}{q}\ln\left(\frac{np}{n_i^2}\right)\right]$;[28] therefore, the potential drop (i.e., $V_{Joule} = V_{bi} - V$) in depletion region

can be expressed by

$$V_{Joule} = \frac{k_BT}{q}\ln\left(\frac{N_aN_d}{n_i^2}\right) - \frac{k_BT}{q}\ln\left(\frac{np}{n_i^2}\right) \\ = \frac{k_BT}{q}\ln\left(\frac{N_aN_d}{np}\right) = \frac{k_BT}{q}\ln\left(\frac{\gamma N_aN_d}{G}\right) \quad (6)$$

where n_i is the intrinsic carrier density and N_d (N_a) the doping concentration of donor (acceptor). It can be seen that this potential drop is caused by the energy band bending, which is determined by the doping concentration, carrier recombination and generation rate. ii) For the potential drop at the metal–semiconductor interface, it is determined by the energy difference between the conduction/valance and corresponding quasi-Fermi level. Generally, the photogenerated electrons (Δn) and holes (Δp) collected by electrodes are far less than the background doping ($\Delta n \ll N_d$, $N_d + \Delta n \approx N_d$ and $\Delta p \ll N_a$, $N_a + \Delta p \approx N_a$).[28] Therefore, the lost potential of electron/hole at the metal–semiconductor interface can be calculated respectively by

$$\Delta\varphi_n = E_c - E_{Fn} = -k_BT\ln\left(\frac{N_d}{N_c}\right) \quad (7)$$

$$\Delta\varphi_p = E_{Fp} - E_v = -k_BT\ln\left(\frac{N_a}{N_v}\right) \quad (8)$$

iii) The potential drop at the heterojunction interface arises from the energy band offsets. Therefore, the energy band alignment is an essential optimization strategy.

3. Analytically Tracing the Energies in Double-Junction SCs

Based on the aforementioned analysis for single-junction SC, the double-junction SC can also be studied in a similar way (see S2, Supporting Information). For a double-junction SC in four-terminal configuration, the carrier thermodynamic loss is from both subcells. However, for the two-terminal system, the tunnel junction is the key to electrically connect the subcells. **Figure 2** shows the energy band diagram and carrier transportation in a two-terminal double-junction SC, which is consisted of two nip subcells. Under illumination, the photogenerated holes are transported to the hole transport layer (HTL) of top SC and photogenerated electrons to the electron transport layer (ETL) of bottom SC driven by the built-in electric fields in the subcells. It should be noted that the photogenerated carriers accumulated at the sides of tunnel junction will tunnel to a low-energy position, leading to a voltage decrease in ΔE due to the tunneling effect (see Figure 2). Moreover, only if the magnitudes of electrons and holes accumulated at the HTL of top SC and ETL of bottom SC are identical, there is no extra carrier recombination; that is to say, the current matching is essential in two-terminal double-junction SC. In this ideal case, the sum of Joule and Peltier heats in two-terminal double-junction SC can be expressed as
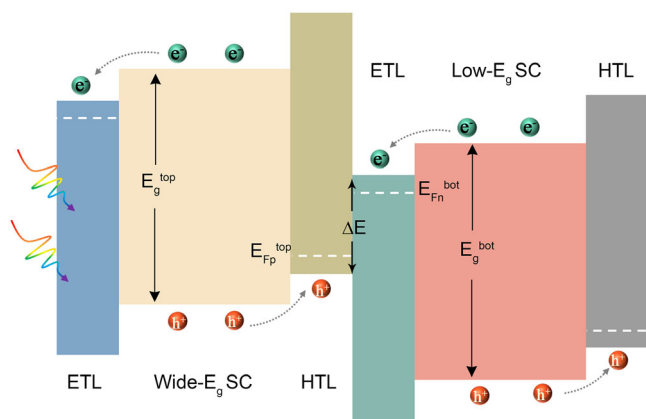
Figure 2. The schematic diagram of a double-junction SC consisted by two nip subcells.

$$H_{\text{Joule}} + H_{\text{Peltier}}^{\text{SM}} + H_{\text{Peltier}}^{\text{SS}} = (E_g^{\text{top}}/q + E_g^{\text{bot}}/q + 3k_BT - qV) \cdot J/q \tag{9}$$

In the double-junction SC system, the sum of Joule and Peltier heats are attributed to the bandgaps of both subcells, the current within the two-terminal SC and the forward bias.

For the photovoltaic system, the photogenerated current J_{ph}, recombination current J_{rec} (the sum of bulk and surface recombinations), and output current satisfy the current conservation relationship: $J_{\text{ph}} = J_{\text{rec}} + J$.[22] Thus, we can find that the incident photon energy is identical to the sum of six kinds of carrier energy losses and electrical output. The corresponding energy conservation requires

$$h\nu \cdot J_{\text{ph}}/q = (h\nu - E_g - 3k_BT) \cdot J_{\text{ph}}/q + (E_g + 3k_BT - qV)$$
$$\cdot J/q + (E_g + 3k_BT) \cdot J_{\text{rec}}/q + J \cdot V \tag{10}$$

4. Results and Discussion

4.1. Efficiency Limit of Single-Junction SCs

Based on the aforementioned analytical study on the energy losses in SCs, the power densities (as well as their fractions) of the various energy-conversion processes as the functions of material bandgap are shown in **Figure 3**a. It can be clearly seen that the incident solar power is completely consumed by the rich OET processes, i.e., the optical transmission ($P_{h\nu} < E_g$), heats (thermalization, recombination, Joule, and Peltier heats) and electrical output. Particularly, the thermalization (transmission) loss significantly consumes the solar power in narrow-bandgap (wide-bandgap) system. The other noticeable energy losses are from the Joule and Peltier heats, especially for the narrow-bandgap SCs, as shown in Figure 3a. The recombination loss is not as high as other factors, but also shows a higher value under a narrower bandgap due to the stronger blackbody radiation.

Examining the energy losses under various bandgaps, it shows that the SC with the bandgap of 1.34 eV achieves the maximum

efficiency of 33.7%. For more detailed bandgap-dependent energy conversion characteristics, the fractions of the various energy-conversion processes of SCs are listed in **Table 1**, e.g., for Si (1.12 eV), GaAs (1.4 eV), and perovskite (1.55 eV) materials. It is found that about 20% of the absorbed solar energy is consumed by the recombination, Joule and Peltier heats for all SCs with any material bandgaps, as shown in Figure S1, Supporting Information. Thus, the wide-bandgap SC shows the superior conversion capability for the absorbed solar power due to the lower thermalization loss, as shown in Figure S1, Supporting Information.

The power densities (as well as their fractions) of the various energy-conversion processes as the functions of the forward bias are shown in Figure 3b, where the SC with bandgap of 1.55 eV (e.g., perovskite) is taken as an example. 1) The thermalization heat is obviously independent of the forward bias. 2) At the short-circuit point ($V = 0$), the solar energy is consumed completely by the thermalization, recombination, Joule and Peltier heats without any electrical output. 3) With increasing the forward bias, the weakened built-in electric field leads to a reduced current, so that the decreased Joule and Peltier losses. 4) Under the open-circuit point, the overall energy is lost through the thermalization and bulk recombination. Similar studies have also been conducted for Si and GaAs SCs in Figures S2, Supporting Information, which exhibits the similar carrier characteristics.

4.2. Extrinsic Energy Losses in Single-Junction SCs

Actually, the photovoltaic materials do not own the ideal properties as expected in calculating the limiting efficiencies. The realistic factors include the poor carrier transports (e.g., high recombination) and device configurations (e.g., low doping concentration, misalignment of energy band), which degrade the performance of SC.[29–31] We now focus on the effects of these factors on the carrier thermodynamic characteristics of SCs (e.g., perovskite with bandgap of 1.55 eV). For an ideal SC, the intrinsic energy losses have a minimize value at the maximum power point. With considering an extrinsic recombination (e.g., carrier lifetime $\tau = 5\,\mu s$), the lost electricity will be converted into heats, mostly into Joule heat, as shown in **Figure 4**a. Moreover, the relatively large recombination losses are obtained in narrow-bandgap SCs due to a higher SRH recombination ($n_i \approx e^{-E_g/k_BT}$), as shown in Figure S3, Supporting Information.

Figure 4b shows the bias-dependent power densities of ideal ($\tau = \infty$) and practical ($\tau = 5\,\mu s$) perovskite SCs, where we can also discover that the lost electricity goes completely into the various heats. Here, we comparably analyze the bias-dependent energy components for the ideal and realistic SCs. It can be observed that: 1) the thermalization-induced loss is only dependent with the bandgap of SC, therefore, the P_{therma} is a constant value for SC with a specific bandgap and irrespective to the applied bias. 2) Comparing for the ideal SC, the extrinsic recombination of carrier undoubtedly leads to the increase of recombination heats for the realistic SC. Increasing forward bias, the weakened built-in electric field can hardly transport effectively the photogenerated carrier leading to an increased recombination current, certainly, an increased recombination heat (P_{Rec}) is observed
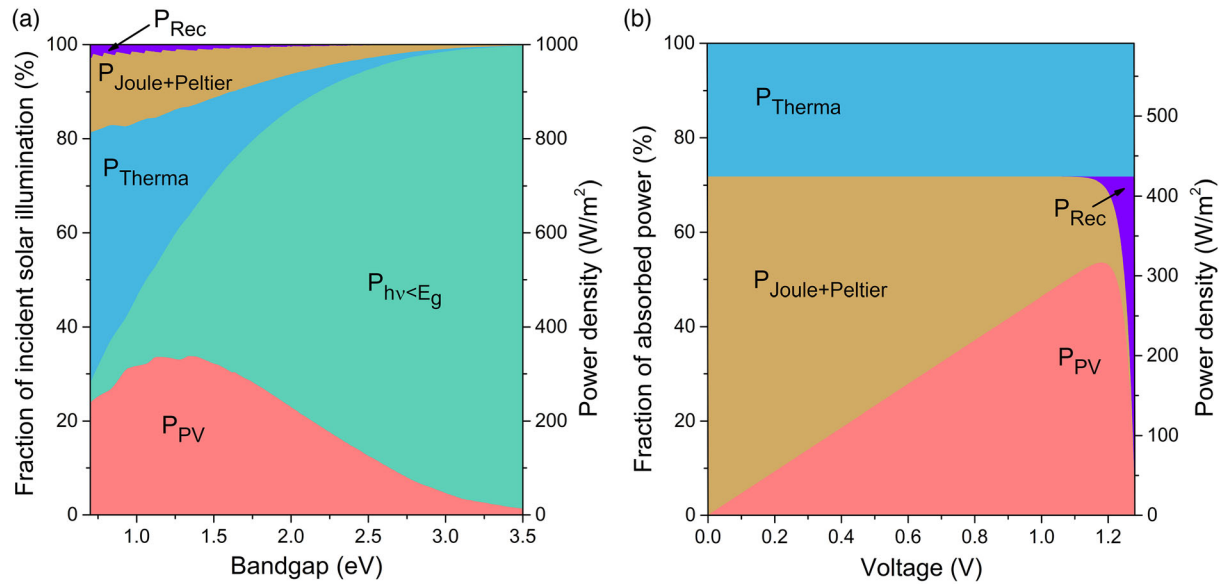
Figure 3. The proportions and power densities of various energy conversion processes as the function of a) the bandgap of SC and b) the electrical bias with an AM 1.5 solar incidence. In (b), the perovskite SC with $E_g \approx 1.55$ eV is considered.

Table 1. The power densities under various energy-conversion processes and their fractions for Si, GaAs, and perovskite SCs.

		P_{Abs}	P_{Therma}	$P_{Joule+Peltier}$	P_{Rec}	P_{PV}
Si (1.12 eV)	Power density	808.08	317.16	139.9	16.11	334.91
	Fraction		39.25%	17.31%	1.99%	41.45%
GaAs (1.4 eV)	Power density	671.6	211.36	115.91	9.46	334.87
	Fraction		31.47%	17.26%	1.41%	49.86%
Perovskite (1.55 eV)	Power density	588.57	166.42	98.75	8.47	314.93
	Fraction		28.27%	16.78%	1.44%	53.51%

with the increase of forward bias, as shown in Figure 4b. 3) As that the extrinsic SRH recombination leads to the decrease in Fermi-level splitting, the increased Joule heat loss is obtained within the realistic SC (see Equation (6)). However, the current density shows a monotonic decrease and V_{oc} shows an exponential decrease under increasing forward bias, so that the Joule heat shows a decline (see Equation (S3), Supporting Information). 4) The Peltier heat is dependent with the current density for a specific SC (see Equation (S4)−(S7), Supporting Information), hence, it changes linearly with the current density. Thus, a reduced $P_{Joule+peltier}$ (sum of Joule and Peltier heats) is observed with increasing forward bias, as shown in Figure 4b.

Figure 4c explores the recombination and light intensity effects on V_{oc}. A high recombination significantly reduces V_{oc} due to the increased Joule and recombination heats. Hence, the fit of light intensity-dependent V_{oc} yields $n = 1 \, k_B T/q$ and $n = 1.98 \, k_B T/q$ for the ideal and practical SCs, respectively. In addition, the V_{oc} increases linearly with the light intensity due to the reduced potential drop in the depletion region (see Equation (6)). As shown in Figure 4d, V_{oc} increases linearly with reducing the energy-band offset or increasing the doping concentration due to the reduced Peltier losses. To summarize the

observations of Figure 4d, a high doping concentration and a small energy band offset are necessary for reducing the potential drop at the metal–semiconductor and heterojunction interfaces, respectively.

4.3. OET Model of SC

Generally, the lost energy increases the operating temperature of SC up to 40−60 °C or higher in outdoor environment.[32,33] The high working temperature significantly degrades the performance of SC; meanwhile, the attenuated performance further heats up the SC. To effectively address the coupling relationship between the temperature and performance of SC, we develop a coupled OET model for photovoltaic systems. The stable working temperature of SC can be obtained after reaching the thermodynamic equilibrium between heat generation and dissipation[32]

$$H_{Therma}(T_{sc}) + H_{Joule+Peltier}(T_{sc}) + H_{rec}(T_{sc}) - H_{out}(T_{sc}, T_{amb}) = 0 \tag{11}$$

where $H_{out} = h_c \cdot (T_{SC} - T_{amb})$ denotes the heat dissipation process due to the convection and conduction effects, h_c the heat exchange coefficient of convection and conduction, and T_{SC} ($T_{amb} = 300$ K) the SC (ambient) temperature. Here, it should be noted that the radiation recombination is not obtained in the $H_{rec}(T_{sc})$ since it radiates photons without heating the SC.

The operating temperature of SC as the function of SC bandgap is shown in **Figure 5**a. Due to the higher thermalization loss generated in a low-bandgap SC, a higher operating temperature can be observed. For instance, the operating temperatures of Si, GaAs, and perovskite SCs are 57.1, 43.9, and 40.3 °C, respectively, which agree well with the experimental measurements.[32–34] In addition, we investigate the environmental effect (e.g., heat convection and conduction effects) on the working temperature of SC. Certainly, the stronger heat convection and conduction dissipation
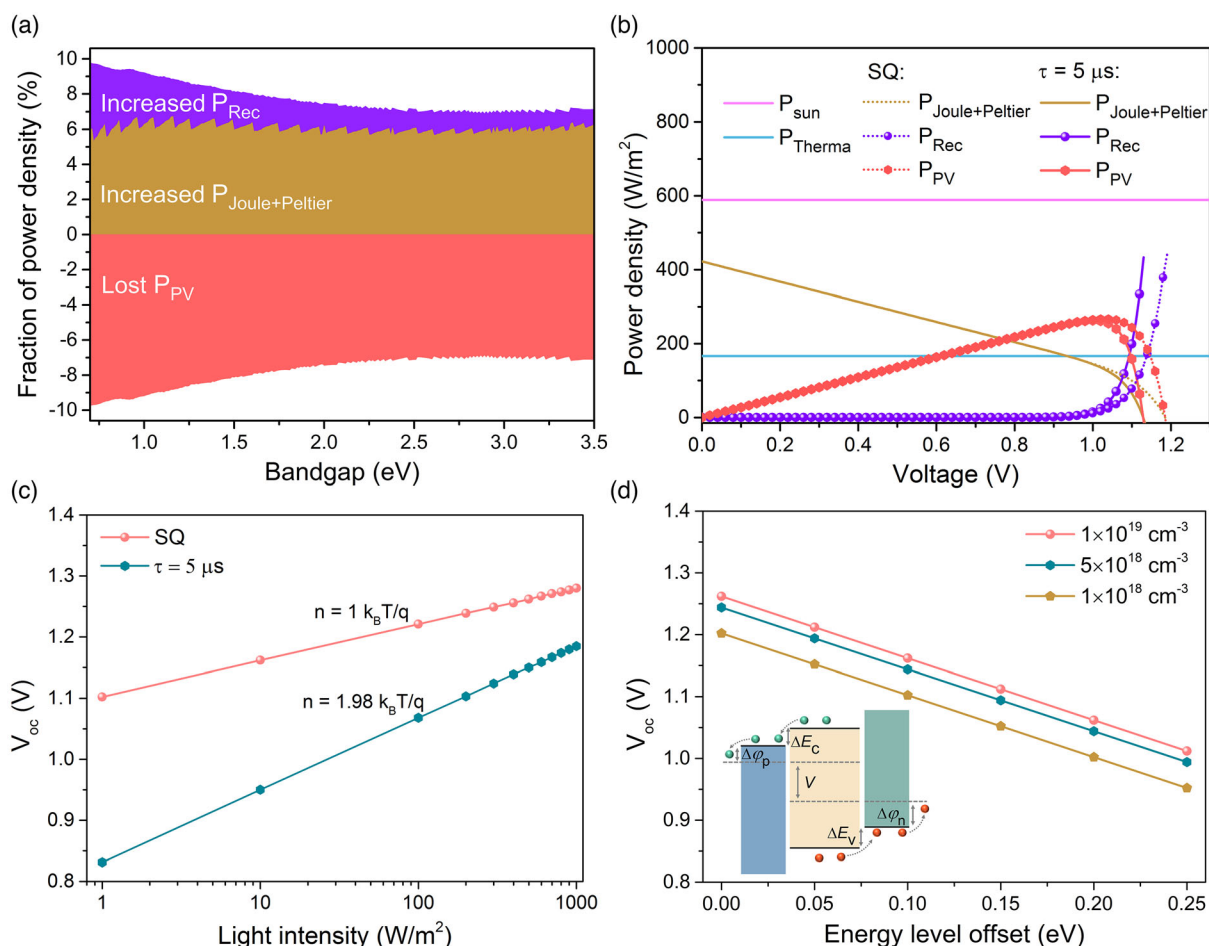
Figure 4. a) The fraction of lost electricity and converted into the recombination, Joule and Peltier heats after considering the extrinsic SRH recombination. b) The bias-dependent power densities for various energy-conversion mechanisms, where the ideal and practical SCs are considered. c) The light intensity effect on V_{oc}, where both ideal and realistic ($\tau = 5\ \mu s$) SCs are considered for comparison. d) The energy band offset and doping concentration effects on the influence of V_{oc}.
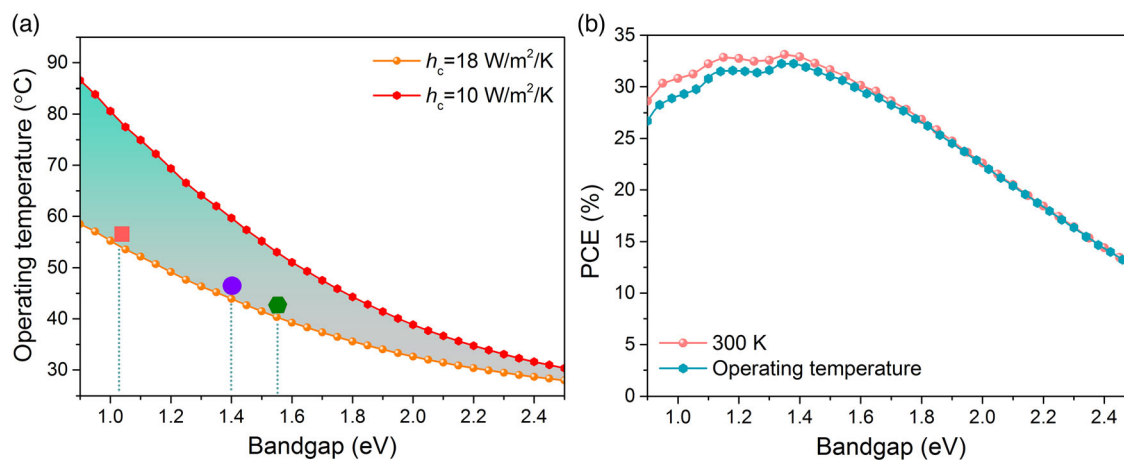

Figure 5. a) The estimated operating temperature of ideal single-junction SC as the function of bandgap of photovoltaic material, where $h_c = 18$ and $10\ W\ m^{-2}\ K^{-1}$ are considered for comparison. The red, purple, and green labels represent the experimentally measured working temperatures of typical Si, GaAs, and perovskite SCs, respectively. b) The efficiency limit of single-junction SC under the ideal (300 K) and practical working temperature, respectively.

(e.g., $h_c = 18\,\text{W}\,\text{m}^{-2}\,\text{K}^{-1}$) can guarantee a lower working temperature of SC, as shown in Figure 5a. Based on the coupled OET model, the efficiency limit of SCs under a realistic working temperature can also be estimated, as shown in Figure 5b, where the efficiency limit of an ideal SC ($T_{sc} = 300\,\text{K}$) is plotted for comparison. It can be clearly seen that the temperature effect significantly degrades the performance of SC due to the increased radiative recombination loss. Since the higher temperature is obtained in low-bandgap SC, a remarkable reduction in power conversion efficiency (PCE) is observed. The efficiency limit of 32.2% is achieved for the device with the bandgap of 1.38 eV, which is 1.5% lower than the ideal case.

4.4. Limiting Efficiency and Energy Losses in Double-Junction SCs

The aforementioned study on the single-junction SC can be further extended for the double-junction system. Here, we consider two kinds of double-junction SCs (i.e., perovskite/Si and perovskite/perovskite setups) under two- or four-terminal configurations. **Figure 6**a shows the efficiency limits of two- and four-terminal Si/perovskite double-junction SCs as the functions of the bandgap of top perovskite. Here, the carrier lifetime $\tau = 5\,\mu\text{s}$ is introduced to match the experiment efficiency of single-junction SC (Figure S3, Supporting Information). In this case, the efficiencies of practical double-junction SCs can be obtained. It is found that a slightly larger bandgap of top SC is essential in practical double-junction systems to achieve the maximum efficiency (comparing for the ideal case, $\tau = \infty$), as shown in Figure 6a. For example, the matching bandgaps of top perovskite material are 1.74 eV (1.81 eV) and 1.76 eV (1.82 eV) for the ideal and practical two- (four-) terminal perovskite/Si double-junction SCs, respectively, as shown in **Table 2**. To explore the energy-conversion processes in double-junction SC, the detailed carrier thermodynamic characteristics are shown in Figure 6b. Obviously, the thermalization loss can be effectively decreased by double-junction design; however, the Joule and recombination losses from two subcells are increased slightly. Finally, the maximum efficiencies of 36.91% and 37.5% can be achieved for the practical two and four-terminal Si/perovskite double-junction SCs, respectively. For the perovskite/perovskite configuration, the best matching bandgaps of top perovskite
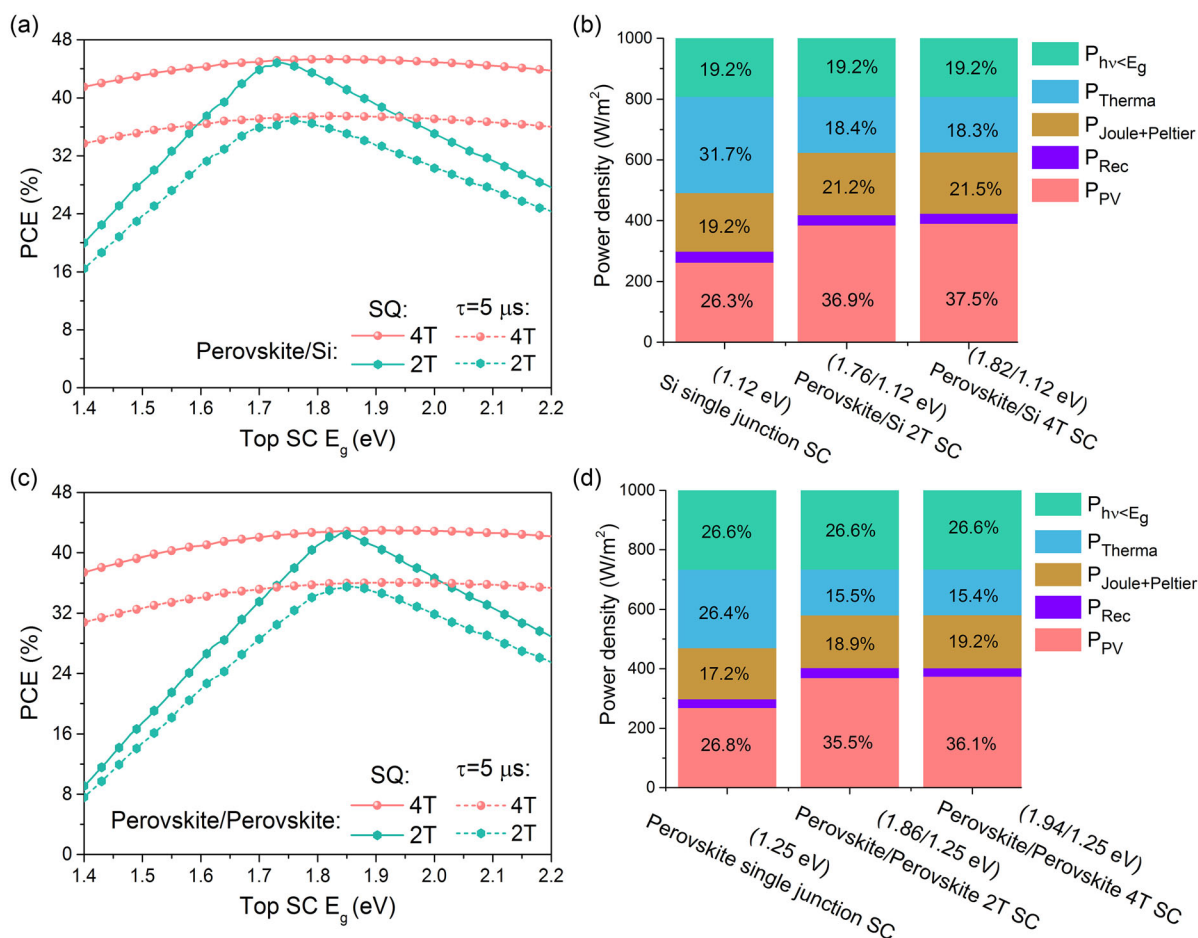

Figure 6. a) The maximum efficiencies of the two- and four-terminal perovskite/Si double-junction SCs as the function of the bandgap of top perovskite SC. Here, the efficiency limits of ideal and practical SCs are plotted for comparison. b) The carrier thermodynamic characteristics analysis for the practical single-junction Si and Si-based double-junction SCs (e.g., $\tau = 5\,\mu\text{s}$). The replots of (a) and (b) are given in (c) and (d) for perovskite/perovskite double-junction SCs.

Table 2. The efficiency limits of the two- and four-terminal perovskite/Si and perovskite/perovskite double-junction SCs.

	Perovskite/Si 2T double junction		Perovskite/Si 4T double junction		Perovskite/perovskite 2T double junction		Perovskite/perovskite 4T double junction	
	Matched top E_g [eV]	PCE [%]	Matched top E_g [eV]	PCE [%]	Matched top E_g [eV]	PCE [%]	Matched top E_g [eV]	PCE [%]
Ideal SC	1.74	44.82	1.81	45.35	1.84	42.60	1.92	42.96
Realistic SC	1.76	36.91	1.82	37.5	1.86	35.61	1.94	36.08

are 1.86 and 1.94 eV for the practical two and four-terminal double-junction SCs, respectively, so that the maximum efficiencies of 35.61% and 36.08% can be achieved (see Figure 6c,d). Further, we estimate the operating temperatures of the four- and two-terminal double-junction SCs, as shown in Figure S4a,b, Supporting Information, respectively. Compared with the single-junction, there is no doubt that the double-junction SC has a lower operating temperature. For example, the temperature of four and two-terminal Si-based double-junction SCs are only 44.69 and 44.99 °C respectively, which are ≈12 °C lower than the single-junction Si SC.

5. Conclusion

We focused on tracing the energies in photovoltaic devices by analytically quantifying the microscopic energy conversion channels and numerically addressing the OET responses of both single- and double-junction SCs. From the carrier thermodynamic perspective, we demonstrated six categories of intrinsic energy losses and three categories of electrical potential losses within SCs. It was found that the drops of V_{oc} are primarily from the Joule and Peltier losses, which however can be effectively regulated by optimizing the recombination, doping concentration and energy band alignment. We then examined how the energy losses influence the temperature responses of the SCs through an advanced multiphysics simulation. Based on the developed the OET model of SC, the energy-based analysis was carried out for single- and double-junction SCs. This uncovered the detailed energy distributions in the discussed SCs, especially in Si/perovskite and perovskite/perovskite double-junction SCs. It was found that a slightly higher (compared with the ideal system) bandgap of top SC should be adopted for the design of double-junction SCs, which show an efficiency up to 37.5% by the optimally designed Si/perovskite combination. This study provides a deeper insight into the fundamental thermodynamics within SCs, which is beneficial for understanding the fundamental physics of photovoltaics and guiding the design of high-performance SCs.

Supporting Information

Supporting Information is available from the Wiley Online Library or from the author.

Acknowledgements

Conflict of Interest

The authors declare no conflict of interest.

Data Availability Statement

Research data are not shared.

Keywords

[1] K. Yoshikawa, H. Kawasaki, W. Yoshida, T. Irie, K. Konishi, K. Nakano, T. Uto, D. Adachi, M. Kanematsu, H. Uzu, K. Yamamoto. *Nat. Energy* **2017**, *2*, 17032.

[2] M. A. Green, E. D. Dunlop, J. Hohl-Ebinger, M. Yoshita, N. Kopidakis, X. Hao. *Prog. Photovolt. Res. Appl.* **2020**, *28*, 629.

[3] M. Kim, G. Kim, T. K. Lee, I. W. Choi, H. W. Choi, Y. Jo, Y. J. Yoon, J. W. Kim, J. Lee, D. Huh, H. Lee, S. K. Kwak, J. Y. Kim, D. S. Kim. *Joule* **2019**, *3*, 2179.

[4] J. Xu, C. C. Boyd, Z. J. Yu, A. F. Palmstrom, D. J. Witter, B. W. Larson, R. M. France, J. Werner, S. P. Harvey, E. J. Wolf, W. Weigand, S. Manzoor, M. F. A. M. Hest, J. J. Berry, J. M. Luther, Z. C. Holman, M. D. McGehee. *Science* **2020**, *367*, 1097.

[5] A. Al-Ashouri, E. Köhnen, B. Li, A. Magomedov, H. Hempel, P. Caprioglio, J. A. Marquez, A. B. M. Vilches, E. Kasparavicius, J. A. Smith, N. Phung, D. Menzel, M. Grischek, L. Kegelmann, D. Skroblin, C. Gollwitzer, T. Malinauskas, M. Jost, G. Matic, B. Rech, R. Schlatmann, M. Topic, L. Korte, A. Abate, B. Stannowski, D. Neher, M. Stolterfoht, T. Unold, V. Getautis, S. Albrecht. *Science* **2020**, *370*, 1300.

[6] J. F. Geisz, R. M. France, K. L. Schulte, M. A. Steiner, A. G. Norman, H. L. Guthrey, M. R. Young, T. Song, T. Moriarty. *Nat. Energy* **2020**, *5*, 326.

[7] W. Shockley, H. J. Queisser. *J. Appl. Phys.* **1961**, *32*, 510.

[8] A. D. Vos. *J. Phys. D: Appl. Phys.* **1980**, *13*, 839.

[9] L. C. Hirst, N. J. Ekins-Daukes. *Prog. Photovolt. Res. Appl.* **2011**, *19*, 286.

[10] S. R. Cowan, A. Roy, A. J. Heeger. *Phys. Rev. B* **2010**, *82*, 245207.

[11] J. C. Blakesley, D. Neher. *Phys. Rev. B* **2011**, *84*, 075210.

[12] Y. Zhao, C. Liang, M. Sun, Q. Liu, F. Zhang, D. Li, Z. He. *J. Appl. Phys.* **2014**, *116*, 154506.

[13] N. K. Elumalai, A. Uddin. *Energy Environ. Sci.* **2016**, *9*, 391.

[14] P. Caprioglio, M. Stolterfoht, C. M. Wolff, T. Unold, B. Rech, S. Albrecht, D. Neher. *Adv. Energy Mater.* **2019**, *9*, 1901631.

[15] S. Wang, T. Sakurai, W. Wen, Y. Qi. *Adv. Mater. Interfaces* **2018**, *5*, 1800260.

[16] M. Stolterfoht, P. Caprioglio, C. M. Wolff, J. A. Marquez, J. Nordmann, S. Zhang, D. Rothhardt, U. Hormann, Y. Amir, A. Redinger, L. Kegelmann, F. Zu, S. Albrecht, N. Koch, T. Kirchartz, M. Saliba, T. Unold, D. Neher. *Energy Environ. Sci.* **2019**, *12*, 2778.

[17] X. Li, N. P. Hylton, V. Giannini, K. H. Lee, N. J. Ekins-Daukes, S. A. Maier. *Opt. Express* **2011**, *19*, A888.

[18] X. Li, N. P. Hylton, V. Giannini, K. H. Lee, N. J. Ekins-Daukes, S. A. Maier. *Prog. Photovolt. Res. Appl.* **2013**, *21*, 109.

[19] L. Chen, S. Wu, D. Ma, A. Shang, X. Li. *Nano Energy* **2018**, *43*, 177.

[20] A. Shang, Y. An, D. Ma, X. Li. *AIP Adv.* **2017**, *7*, 085019.

[21] A. Shang, X. Li. *Adv. Mater.* **2017**, *29*, 1603492.

[22] Y. An, C. Wang, G. Cao, X. Li. *ACS Nano* **2020**, *14*, 5017.

[23] A. Polman, M. Knight, E. C. Garnett, B. Ehrler, W. C. Sinke. *Science*, **2016**, *352*, aad4424.

[24] R. Rawat, R. Lamba, S. C. Kaushik. *Renewable Sustainable Energy Rev.* **2017**, *71*, 630.

[25] A. Polman, A. A. Harry. *Nat. Mater.* **2012**, *11*, 174.

[26] J. Guillemoles, T. Kirchartz, D. Cahen, U. Rau. *Nat. Photonics* **2019**, *13*, 501.

[27] G. K. Wachutka. *IEEE Trans. Comput. Aid. Des.* **1990**, *9*, 1141.

[28] S. M. Sze, *Physics of Semiconductor Devices*, 3rd ed., John Wiley & Sons, New York **2007**.

[29] Y. An, A. Shang, G. Cao, S. Wu, D. Ma, X. Li. *Sol. RRL* **2018**, *2*, 1800126.

[30] L. Huang, D. Zhang, S. Bu, R. Peng, Q. Wei, Z. Ge. *Adv. Sci.* **2020**, *7*, 1902656.

[31] A. Ren, H. Lai, X. Hao, Z. Tang, H. Xu, B. M. F. Y. Jeco, K. Watanabe, L. Wu, J. Zhang, M. Sugiyama, J. Wu, D. Zhao. *Joule* **2020**, *4*, 1263.

[32] Y. An, C. Sheng, X. Li. *Nanoscale* **2019**, *11*, 17073.

[33] X. Sun, T. J. Silverman, Z. Zhou, M. R. Khan, P. Bermel, M. A. Alam. *IEEE J. Photovolt.* **2017**, *7*, 566.

[34] M. Jost, B. Lipovsek, B. Glazar, A. Al-Ashouri, K. Brecl, G. Matic, A. Magomedov, V. Getautis, M. Topic, S. AlbrechtJot. *Adv. Energy Mater.* **2020**, *10*, 2000454.